Journal of Energy Storage 73 (2023) 108893

Contents lists available at ScienceDirect

Journal of Energy Storage

journal homepage: www.elsevier.com/locate/est

Research papers

Latent heat thermal energy storage in a shell-tube design: Impact of metal foam inserts in the heat transfer fluid side

Mehdi Ghalambaz [a], Mikhail Sheremet [b], Zehba Raizah [c], Nevzat Akkurt [d], Mohammad Ghalambaz [b,*]

[a] College of Engineering, Almaaqal University, Basra 61003, Iraq
[b] Laboratory on Convective Heat and Mass Transfer, Tomsk State University, 634050 Tomsk, Russia
[c] Department of Mathematics, Faculty of Science, King Khalid University, Abha 62529, Saudi Arabia
[d] Department of Mechanical Engineering, Munzur University, 62000 Tunceli, Turkey

ARTICLE INFO

Keywords:
Latent heat thermal energy storage
Shell-tube
Metal foam inserts
Heat transfer fluid
Phase change materials

ABSTRACT

The improvement of heat transfer in latent heat thermal energy storage (LHTES) system is a crucial task. In the current study, the impact of diverse metal foam (MF) layer arrangements on heat transfer fluid (HTF) within a shell-tube LHTES is explored. Six distinct cases (A-F) with varied MF coverage percentages and layer dimensions were assessed. The local thermal non-equilibrium model was utilized to take into account the PCM and MF temperatures. The finite element method was used for solving the partial differential equations. The impact of MF configurations and inlet pressures (250 Pa, 500 Pa, and 750 Pa) on the thermal energy storage/release was addressed. Cases A-C, featuring a 50 % MF concentration, exhibit shorter melting times than Cases D—F, with decreasing MF concentrations. A higher MF concentration improves the melting process due to increased thermal conductivity and lower thermal resistance on the HTF side. Cases D—F, with a centralized MF layer and decreasing concentrations from 25 % to 6.25 %, display progressively shorter melting times, suggesting that a lower MF concentration leads to more efficient melting. Solidification times also decrease with increasing inlet pressures across all cases. Reynolds numbers, influenced by average HTF tube outlet velocity, vary substantially across cases and inlet pressure differences. Cases A-C demonstrate similar Reynolds numbers for each inlet pressure difference, while Cases D—F show a more pronounced increase in Reynolds numbers as the MF layer is reduced and flow resistance drops. Cases A (50 % MF layer) and F (6.5 % MF layer) provide the quickest charging and discharging times due to their unique combination of MF layer properties and inlet pressures. The study highlights the need to consider MF layer composition and inlet pressure when designing optimal LHTES systems for efficient energy storage/release.

1. Introduction

In recent years, Latent Heat Thermal Energy Storage (LHTES) has garnered considerable interest due to its potential to address energy efficiency and sustainability issues. Effective use of LHTES systems can result in substantial energy savings, decreased greenhouse gas emissions, and enhanced energy management [1,2]. The heat transfer fluid (HTF) is one of the primary components of LHTES systems and serves a crucial role in transferring heat between different components. Metal foam (MF) inserts can substantially enhance the efficacy of high-temperature foams (HTFs). This article aims to provide insights into the use of MF inserts in LHTES systems, specifically in a shell-tube design, and their effect on the HTF side.

LHTES enables the storage and retrieval of thermal energy by utilizing the latent heat associated with phase change materials (PCMs) [3,4]. The high energy density of PCMs enables a more compact storage system when compared to sensible heat storage methods, resulting in reduced space requirements and potential cost savings [4]. LHTES systems have been utilized successfully in various applications, including waste heat recovery, solar energy storage, building heating and ventilation, and thermal management of electronic devices [5].

In recent years, the need to integrate renewable energy sources, such

* Corresponding author.
E-mail addresses: ghalambaz.mehdi@gmail.com (M. Ghalambaz), sheremet@math.tsu.ru (M. Sheremet), zaalrazh@kku.edu.sa (Z. Raizah), nevzatakkurt@gmail.com (N. Akkurt), m.ghalambaz@gmail.com (M. Ghalambaz).

https://doi.org/10.1016/j.est.2023.108893
Received 10 June 2023; Received in revised form 26 August 2023; Accepted 31 August 2023

as solar and wind power, into the energy infrastructure has fueled interest in LHTES. To ensure a stable energy supply, the intermittent nature of these energy sources necessitates the development of efficient and dependable energy storage solutions [6,7]. LHTES systems offer a valuable means of storing excess energy generated during periods of high supply and releasing it during periods of high demand, thereby improving the overall efficiency of the energy system [8].

One of the primary challenges associated with LHTES is the relatively low thermal conductivity of the majority of PCMs, resulting in sluggish charging and discharging rates and limiting the system's overall efficacy [9]. Researchers have investigated various approaches such as using nano-additives [10], dynamic phase change [11,12], nano-encapsulation [13,14], metal foams [15] and fins [16]. Among these approaches, MFs are a promising candidate for improving the thermal conductivity of PCMs and circumvent the low thermal conductivity limitation [15,17]. MFs are porous materials with a high surface area-to-volume ratio, exceptional mechanical properties, and good thermal conductivity [9,18].

It has been demonstrated that the incorporation of MFs into PCMs substantially improves the thermal conductivity of the PCM, resulting in quicker charging and discharging rates and improved overall LHTES system performance [10]. In addition, MFs can offer structural support for PCMs, preventing leakage and deformation during phase transitions [19,20]. Recent research has demonstrated the efficacy of MFs in a variety of LHTES applications, including waste heat recovery [21,22] and solar energy storage [23].

Heat exchangers are essential components of LHTES systems because they facilitate heat transfer between the PCM and HTF. The thermal conductivity of the materials used and the overall design of heat exchangers [24] can have a substantial effect on their efficacy. Due to their high thermal conductivity, large surface area, and low-pressure drop, MFs have been identified as promising materials for enhancing the efficiency of heat exchangers [17,25].

It has been demonstrated that the use of MFs in heat exchangers improves heat transfer performance by increasing the effective heat transfer area, which results in higher heat transfer coefficients [26,27]. This improvement in heat transfer performance can result in more effective LHTES systems with quicker charging and discharging rates [23]. Recent studies on the use of MFs in various LHTES designs, such as shell-and-tube [28], plate [29], and finned-tube configurations [30], have demonstrated significant enhancements in heat transfer efficiency.

While it has been demonstrated that incorporating MFs into LHTES systems improves heat transfer performance, it is essential to consider the cost and weight implications of their use. MFs can be relatively expensive and add weight to a system, which may negate some of the advantages of enhanced heat transfer performance [31,32]. Therefore, it is essential to optimize the quantity of metal insulation used in the system to accomplish the intended performance enhancement while mitigating the added cost and weight.

Recent studies have investigated the use of small quantities of MF to accomplish significant improvements in heat transfer performance without substantially increasing the system's cost or weight [17,33]. These studies have emphasized the significance of choosing the proper MF partial layer and MF characteristics, such as pore size, porosity, and thermal conductivity in the PCM domain, to accomplish the desired performance enhancements while minimizing material requirements. Additional research can help identify the optimal configurations and designs for MFs used in various LHTES applications.

Shell-tube LHTES units are a prevalent variety of LHTES design that employs a shell-and-tube heat exchanger with the PCM on one side and the HTF flowing through another side [34,35]. This design offers several benefits, such as the ability to accommodate a wide variety of HTF and PCM materials, the simplicity of manufacturing and assembly, and the scalability of larger systems [36]. Recent research has centered on improving the design of shell-tube LHTES systems to enhance system performance and efficiency [34,37]. Diverse strategies, such as the use of finned tubes, enhanced heat transfer surfaces, and the incorporation of MFs within the PCM, have been investigated [29,30,37,38]. These investigations have demonstrated the potential for significant enhancements in the shell-tube LHTES's heat transfer performance, resulting in more compact and efficient energy storage systems.

Using MFs for LHTES in shell-tube configuration has been investigated in several published investigations [34,37–42]. Nonetheless, the enhancement in heat transmission in LHTES is a combination of heat transfer in the HTF, tube exterior, and MF-PCM domain. A significant enhancement in heat transmission on the HTF side could be crucial for pairing with the MF-PCM domain. Thus, the present study investigates for the first time the effect of employing numerous MF layers on the HTF side. For an equitable comparison of the investigated designs, the inlet pressure was assumed to be constant. Using MF inserts on the HTF side of shell-tube LHTES systems may improve the heat transfer to HTF, while the performance of MF can be boosted or limited by the heat transfer capability of the PCM side. The results of this study will contribute to the ongoing development and optimization of LHTES systems, with the aim of improving the efficacy and efficiency of these systems for a broad variety of applications.

2. Physical model

The depiction of a concentrated solar heating system for building heating exemplifies the significance of LHTES in the advancement of solar energy technology. This is because solar energy depends on weather and time and, thus, is intermittent. An LHTES can stock a substantial amount of energy at fusion temperature in a small volume, thereby reducing energy fluctuations in transitory solar energy systems. The system comprises a solar collector, storage tank, LHTES unit, and circulating pumps. The collector heats water and stores it as sensible heat in the hot water tank, which provides hot water as required by the

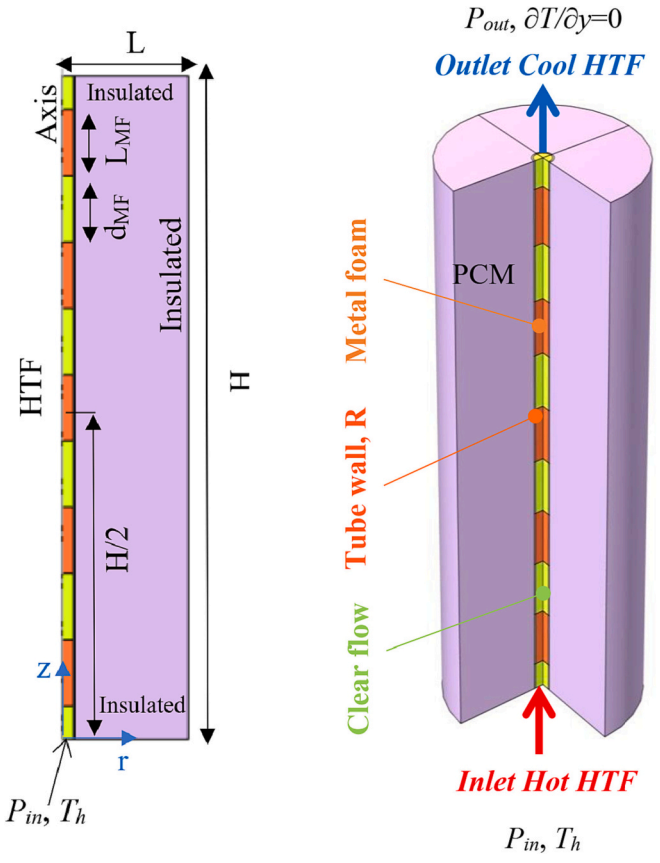

Fig. 1. The physical domain and model configuration.

structure.

Additionally, an auxiliary cycle connects the hot water storage tank to the LHTES unit. During low energy demand or high energy production, the pump in the auxiliary energy storage loop becomes active and transfers the excess heat to the LHTES unit. Conversely, when solar energy generation is inadequate, the tank extracts energy from the LHTES unit. Fig. 1 portrays a diagram of the system.

Using a shell-tube shape, Fig. 2 depicts the design of a Latent Heat Thermal Energy Storage (LHTES) device. The heat transfer fluid, water, enters the tube at a pressure of P_{in} and leaves at the top outlet at zero pressure. The wall thickness of the tube is t, and its outer radius is R. The tube is made of copper and has an outer radius of R. The tube shell is partly coated with a copper-based heterogeneous MF layer. The foam layer is separated from the shell wall by a void filled with paraffin wax, which experiences a phase transition and stores/releases latent heat energy at T_f. Depending on the discharging/charging operation, water transfers heat to the paraffin wax PCM domain through the tube wall and exits at a higher or lower temperature. Many LHTES units may be connected in parallel, series, or a mix of the two to meet the capacity and demand needs of the cycle shown in Fig. 2. The primary purpose is to examine the heat transfer design of the LHTES unit, which includes a layer of heterogeneous foam.

The heat transfer in the unit is controlled by two sections of heat transfer in the PCM storage unit and the HTF side. Here, a layer of isotropic MF has been added to the HTF tube to boost its heat transfer rate and reduce its storage time. The foam fills 50 % of the tube and can be added in various ways. $T_h = T_f + 15\ ^\circ C$ and $T_c = T_f - 15\ ^\circ C$ are the two temperatures inside the temperature cycle. At a fixed-point temperature of T_h, the hot tank transmits surplus energy to the LHTES unit when its beginning temperature is T_c. Thus, throughout the charging procedure, T_h is considered to be the HTF's intake temperature, and $T_{initial} = T_c$.

Fig. 3 shows several configurations of the MF layers in the tube. In this extension, several configurations of MF layers in the tube, focusing on six distinct cases (Case A-F), were considered. These cases represent different percentages of MF coverage and varied MF layer dimensions. The MF layers are essential in controlling the heat transfer characteristics in the HTF tube, and their configurations directly impact the overall performance. In Case A, the HTF tube is filled with 50 % MF. In this configuration, the MF layer covers half of the tube's height (H), with equally distributed foam layers of length ($L_{MF}=H/10$). The uniform

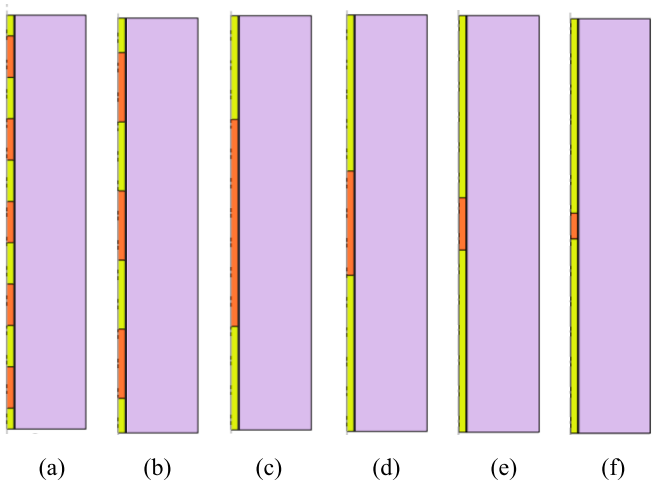

Fig. 3. Various configurations of MF layer in the tube for (a) Case I with 50% MF: L_{MF}=H/10, d_{MF}=H/10; (b) Case II with 50 % MF: L_{MF}=H/6, d_{MF}=H/6; (c) Case III with 50 % MF: L_{MF}=H/2; (d) Case IV with 25 % MF: L_{MF}=H/4; (e) Case IV with 12.5 % MF: L_{MF}=H/8; (f) Case IV with 6.25 % MF: L_{MF}=H/16.

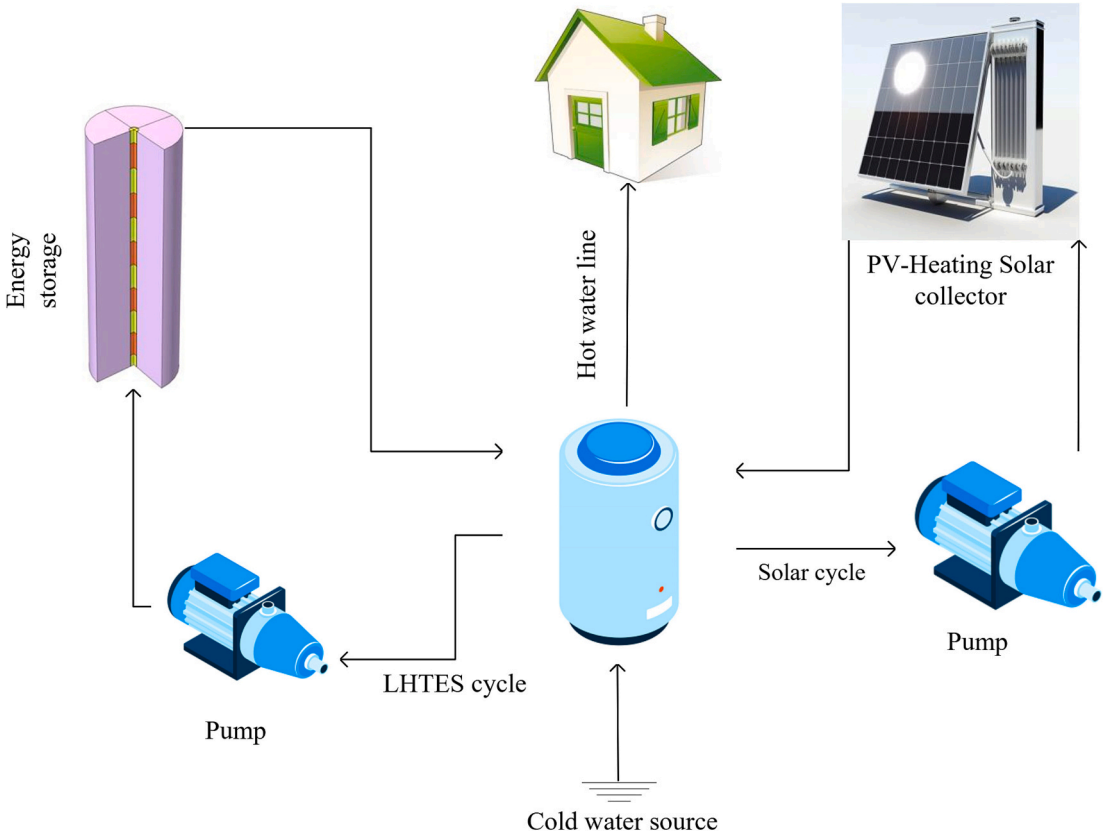

Fig. 2. The application diagram of the LHTES unit in a domestic solar heating cycle.

distribution of the foam layers is expected to improve the heat transfer on the entire HTF side.

Regarding Case B, 50 % of the HTF tube is filled with foam layers. In this case, the MF layer still covers half of the tube's height but with different dimensions: $L_{MF} = H/6$ and $d_{MF} = H/6$. This case also provides a semi-uniform MF distribution. Case C configuration presents an MF layer that covers half of the tube's height but with $L_{MF} = H/2$. This setup creates a single, thick MF layer that spans half the tube's height. Thus, in this case, the foam layer is concentrated along the center. A large pressure drop and small inlet velocity can be expected for all Cases A-C.

In Case D, the MF layer covers a quarter of the tube's height, with $L_{MF} = H/4$. The reduced MF coverage may result in lower heat transfer efficiency and less uniform flow distribution than the previous cases with 50 % MF coverage. However, this configuration can provide lower pressure drops and flow resistance. The smaller the flow resistance, the larger the flow inlet velocity, which may return increases the heat transfer rate. The configuration of Case E features an MF layer covering an eighth of the tube's height (12.5 % MF), with $L_{MF} = H/8$. The reduction in MF coverage may further decrease the heat transfer efficiency and flow uniformity compared to cases with higher MF coverage. However, the pressure drop and flow resistance are expected to be lower in this configuration.

In Case F, the MF layer covers only a sixteenth of the tube's height, with $L_{MF} = H/16$, and MF fills only 6.25 % of the HTF tube. This configuration offers the least MF coverage, which may reduce heat transfer efficiency and non-uniform flow distribution. On the other hand, this setup is expected to provide the lowest pressure drops and flow resistance among all the cases. This case is closest to the clear HTF tube with no MF.

In summary, the various configurations of MF layers in the tube directly impact the heat transfer characteristics, flow distribution, pressure drops, and flow resistance. Higher MF coverage typically leads to enhanced heat transfer and more uniform flow distribution but may also introduce higher pressure drops and flow resistance. Since the inlet pressure is fixed for all cases, an MF layer can reduce the flow rate and negatively impact the heat transfer rate. The present analysis aims to study these trade-offs when selecting the most suitable MF configuration for an LHTES unit.

2.1. Principal equations

The physical model comprises three distinct regions: the HTF, the copper tube wall, and the composite MF-phase change material (MF-PCM). The principal equation for the tube wall (copper) pertains to heat conduction and is articulated as [43–46]:

$$\left(\rho C_p\right)_{\mathrm{Wall}}\frac{\partial T}{\partial t} = k_{\mathrm{Wall}}\left(\frac{\partial^2 T}{\partial z^2}+\frac{1}{r}\frac{\partial}{\partial r}\left(r\frac{\partial T}{\partial r}\right)\right) \tag{1}$$

Here, C_p, ρ, and k denote the specific heat capacity, density, and thermal conductivity of the tube wall, respectively. The time (t) and the temperature field (T) were used in the heat equation. The r- and z-axis introduce the cylindrical coordinate system, as demonstrated in Fig. 2, with the "wall" subscript representing the tube wall.

2.2. HTF principal equations

The local thermal non-equilibrium model is utilized to model the heat transfer in MF in the HTF and PCM domains. The governing equations encompass mass conservation, momentum, and energy for the HTF region:

$$\frac{1}{r}\frac{\partial(ru_r)}{\partial r}+\frac{\partial u_z}{\partial z} = 0 \tag{2}$$

$$\frac{\rho_{\mathrm{HTF}}}{\varepsilon}\left(\frac{\partial u_r}{\partial t}+\frac{1}{\varepsilon}\left(u_z\frac{\partial u_r}{\partial z}+u_r\frac{\partial u_r}{\partial r}\right)\right) = -\frac{\partial p}{\partial r}+\frac{\mu_{\mathrm{HTF}}}{\varepsilon}\left(\frac{1}{r}\frac{\partial}{\partial r}\left(r\frac{\partial u_r}{\partial r}\right)-\frac{u_r}{r^2}+\frac{\partial^2 u_r}{\partial z^2}\right) -\rho_{\mathrm{HTF}}\frac{C_F}{\sqrt{\kappa}}|u|u_r-\frac{\mu_{\mathrm{PCM}}}{\kappa}u_r \tag{3-a}$$

$$\frac{\rho_{HTF}}{\varepsilon}\left(\frac{\partial u_z}{\partial t}+\frac{1}{\varepsilon}\left(u_z\frac{\partial u_z}{\partial z}+u_r\frac{\partial u_z}{\partial r}\right)\right) = -\frac{\partial p}{\partial z}+\frac{\mu_{\mathrm{HTF}}}{\varepsilon}\left(\frac{\partial^2 u_z}{\partial z^2}+\frac{1}{r}\frac{\partial}{\partial r}\left(r\frac{\partial u_z}{\partial z}\right)\right) -\rho_{\mathrm{HTF}}\frac{C_F}{\sqrt{\kappa}}|u|u_z-\frac{\mu_{\mathrm{PCM}}}{\kappa}u_z \tag{4-b}$$

$$\left(\rho C_p\right)_{\mathrm{HTF}}\left(\varepsilon\frac{\partial T_{HTF}}{\partial t}+\left(u_z\frac{\partial T_{HTF}}{\partial z}+u_r\frac{\partial T_{HTF}}{\partial r}\right)\right) = \frac{1}{r}\frac{\partial}{\partial r}\left(\left(k_{td}+k_{\mathrm{eff,HTF}}\right)r\frac{\partial T_{HTF}}{\partial r}\right)+\left(k_{td}+k_{\mathrm{eff,HTF}}\right)\frac{\partial^2 T_{HTF}}{\partial z^2}+h_{sf}A_{sf}\left(T_{\mathrm{MF}}-T_{\mathrm{PCM}}\right) \tag{5-a}$$

$$\left(\rho C_p\right)_{\mathrm{MF}}(1-\varepsilon)\frac{\partial T_{\mathrm{MF}}}{\partial t} = \frac{1}{r}\frac{\partial}{\partial r}\left(k_{\mathrm{eff,MF}}r\frac{\partial T_{\mathrm{MF}}}{\partial r}\right)+\frac{\partial}{\partial z}\left(k_{\mathrm{eff,MF}}\frac{\partial T_{\mathrm{MF}}}{\partial z}\right) -h_{sf}A_{sf}\left(T_{\mathrm{MF}}-T_{\mathrm{HTF}}\right) \tag{6-b}$$

In this case, u_r and u_z denote the velocity components. The dynamic viscosity is symbolized by μ, while the HTF subscript signifies the HTF region. The HTF flow is considered laminar ($Re_{\mathrm{HTF}} \langle 2000$) with $Re_{\mathrm{HTF}} = \rho_{\mathrm{HTF}} \times u \times D/\mu_{\mathrm{HTF}}$ in the tube and $u = \sqrt{(u_r^2+u_z^2)}$. It is important to note that gravity effects are not present in the HTF region, as it is assumed that there is a significant force convection due to the high inlet pressure. In the clear parts of the tube, $\varepsilon \to 0$ and $\kappa \to \infty$ while in the MF parts, the porosity and permeability are the characteristics of the MF.

The effective thermal conductivity (k_{eff}) for MF and HTF fluid is calculated using the following formulas [43,47–49]:

$$k_{eff} = \frac{\sqrt{2}}{2(M_A+M_B+M_C+M_D)} \tag{7}$$

$$M_A = \frac{4\sigma}{\left((2e^2+\pi\kappa(1-e)\right)k_{MF}+\left(4-2e^2-\pi\sigma(1-e)\right)k_{HTF}\right)} \tag{8a}$$

$$M_B = \frac{(\varepsilon-2\sigma)^2}{\left((e-2\sigma)e^2k_{MF}+(2e-4\sigma-e^2(e-2\sigma)\right)k_{HTF}\right)} \tag{8b}$$

$$M_C = \frac{\left(\sqrt{2}-2\sigma\right)^2}{\left(2\pi\sigma^2\left(1-2\sqrt{2}\,e\right)k_{MF}+2\left(\sqrt{2}-2e-\pi\sigma^2\left(1-2\sqrt{2}\,e\right)\right)k_{HTF}\right)} \tag{8c}$$

$$M_D = \frac{2e}{\left(e^2k_{MF}+(4-e^2)k_{HTF}\right)} \tag{8d}$$

$$\sigma = \sqrt{\frac{\sqrt{2}\left(2-\frac{5}{8}\sqrt{2}\,e^3-2\varepsilon\right)}{\left(\pi\left(3-4\sqrt{2}\,e-e\right)\right)}} \tag{8e}$$

$$\sigma = \sqrt{\frac{\sqrt{2}\left(2-\frac{5}{8}\sqrt{2}\,e^3-2\varepsilon\right)}{\left(\pi\left(3-4\sqrt{2}\,e-e\right)\right)}}, e = 0.339 \tag{8f}$$

where the effective thermal conductivities of HTF ($k_{\mathrm{eff,HTF}}$) is obtained by plugging in $k_{\mathrm{MF}} = 0$ in the above equations for the MF regions of the HTF tube. Similarly, the effective conductivity of the MF ($k_{\mathrm{eff,MF}}$) tube is obtained by setting $k_{\mathrm{HTF}} = 0$ in the porous regions of the HTF. The thermal conductivity due to interstitial fluid at the microscopic pore [50] is evaluated following [51]:

$$k_{td} = \frac{0.36}{(1-\varepsilon)}\rho_{HTF}C_pd_{fp}|u| \tag{9a}$$

Following [52], the permeability was also evaluated as:

$$\kappa = \frac{\varepsilon^2}{36}\frac{\left(\sqrt{\frac{\kappa_{tor}}{3\varepsilon}}d_{fp}\right)^2}{\kappa_{tor}(\kappa_{tor}-1)} \tag{9b}$$

where κ_{tor} and d_{fp} are evaluated following:

$$\frac{1}{\kappa_{tor}} = \frac{1}{\varepsilon}\left[\frac{3}{4}+\frac{\sqrt{9-8\varepsilon}}{2}cos\left\{\frac{4}{3}\pi+\frac{1}{3}cos^{-1}\left(\frac{8\varepsilon^2+27-36\varepsilon}{(9-8\varepsilon)^{\frac{3}{2}}}\right)\right\}\right]d_{fp} \tag{10}$$

$$d_{fs} = 1.18\left\{\frac{1}{1-e^{\frac{(\varepsilon-1)}{0.04}}}\right\}\sqrt{\frac{(1-\varepsilon)}{3\pi}}d_{fp} \text{ and } d_{fp} = 0.0254\Big/PPI \tag{11}$$

and for the Frochheimer coefficient [52]:

$$C_F = 0.00212\times\left(\frac{d_{fs}}{d_{fp}}\right)^{-1.63}(1-\varepsilon)^{-0.132} \tag{12}$$

For computing the interface heat transfer between MF and HTF inside the pores, the following relations were employed [47,53]:

$$Nu_{sf} = \begin{cases} 0.76Pr^{0.37}Re_{MF}^{0.4} & 1 \le Re_{MF} \le 40 \\ 0.52Pr^{0.37}Re_{MF}^{0.5} & 40 \le Re_{MF} \le 1000 \\ 0.26Pr^{0.37}Re_{MF}^{0.6} & 1000 \le Re_{MF} \le 10^5 \end{cases}, \tag{13}$$

where $h_{sf} = Nu_{sf}\times k_{sf}/d_{fp}$ and $Re_{MF} = \rho_{HTF}\times d_{sp}\,|u|/(\varepsilon\times\mu_{HTF})$ is the pore Reynolds number. Moreover, $\alpha_{PCM} = k_{PCM}/(\rho C_p)_{PCM}$ and $Pr = \mu_{PCM}\times\rho_{PCM}/\alpha_{PCM}$. The interface surface between pores and the HTF was also computed following [47,53–55]:

$$A_{sf} = \frac{3\pi\left(1-e^{-\frac{(1-\varepsilon)}{0.004}}\right)d_{fs}}{0.59d_{fp}}, \tag{14}$$

2.3. PCM-MF principal equations

The MF-PCM hybrid structure involves the MF, characterized by open cells that enable the molten PCM to circulate through the gaps. Due to variations in the temperature of the molten PCM, buoyancy-induced natural convection could potentially initiate flow movements. Therefore, to simulate phase change free convection heat transfer, it is vital to resolve the equations of mass and momentum conservation, along with the energy conservation for phase change. To represent phase change, the enthalpy porosity technique is applied, which introduces source terms that depend on the volume fraction of melt (φ), enforcing the zero velocities in solidified areas. The model also acknowledges the distinction between the temperature of the PCM and that of the MF porous structure within the pores, leveraging a local-thermal non-equilibrium model to accommodate these variances in temperature. Including non-Darcy influences and key source terms, the main equations governing mass, fluid flow, and energy are formulated accordingly [43–45]:

$$\frac{1}{r}\frac{\partial(ru_r)}{\partial r}+\frac{\partial u_z}{\partial z} = 0 \tag{15}$$

$$\frac{\rho_{PCM}}{\varepsilon}\left(\frac{\partial u_r}{\partial t}+\frac{1}{\varepsilon}\left(u_z\frac{\partial u_r}{\partial z}+u_r\frac{\partial u_r}{\partial r}\right)\right) = -\frac{\partial p}{\partial r}+\frac{\mu_{PCM}}{\varepsilon}\left[\frac{1}{r}\frac{\partial}{\partial r}\left(r\frac{\partial u_r}{\partial r}\right)-\frac{u_r}{r^2}+\frac{\partial^2 u_r}{\partial z^2}\right] -\rho_{PCM}\frac{C_F}{\sqrt{\kappa}}|u|u_r+A_{mush}\frac{(1-\varphi(T))^2}{\lambda_{mush}+\varphi^3(T)}u_r-\frac{\mu_{PCM}}{\kappa}u_r \tag{16-a}$$

$$\frac{\rho_{PCM}}{\varepsilon}\left(\frac{\partial u_z}{\partial t}+\frac{1}{\varepsilon}\left(u_z\frac{\partial u_z}{\partial z}+u_r\frac{\partial u_z}{\partial r}\right)\right) = -\frac{\partial p}{\partial z}+\frac{\mu_{PCM}}{\varepsilon}\left[\frac{\partial^2 u_z}{\partial z^2}+\frac{1}{r}\frac{\partial}{\partial r}\left(r\frac{\partial u_z}{\partial z}\right)\right] -\rho_{PCM}\frac{C_F}{\sqrt{\kappa}}|u|u_z+A_{mush}\frac{(1-\varphi(T))^2}{\lambda_{mush}+\varphi^3(T)}u_z-\frac{\mu_{PCM}}{\kappa}u_z+g\rho_{PCM}\beta_{PCM}(T-T_0) \tag{16-b}$$

$$(\rho C_p)_{PCM}\left(\varepsilon\frac{\partial T_{PCM}}{\partial t}+\left(u_z\frac{\partial T_{PCM}}{\partial z}+u_r\frac{\partial T_{PCM}}{\partial r}\right)\right) = \frac{1}{r}\frac{\partial}{\partial r}\left(k_{eff,PCM}r\frac{\partial T_{PCM}}{\partial r}\right)+\frac{\partial}{\partial z}\left(k_{eff,PCM}\frac{\partial T_{PCM}}{\partial z}\right)-\varepsilon\rho_{PCM}L_{PCM}\frac{\partial\varphi(T)}{\partial t}+h_v(T_{MF}-T_{PCM}) \tag{17-a}$$

$$(\rho C_p)_{MF}(1-\varepsilon)\frac{\partial T_{MF}}{\partial t} = \frac{1}{r}\frac{\partial}{\partial r}\left(k_{eff,MF}r\frac{\partial T_{MF}}{\partial r}\right)+\frac{\partial}{\partial z}\left(k_{eff,MF}\frac{\partial T_{MF}}{\partial z}\right) -h_v(T_{MF}-T_{PCM}) \tag{17-b}$$

The subscripts of eff and MF denote the effective properties and MF, respectively. The latent heat of phase change (L), gravity acceleration (g), porous permeability (κ), Frochheimer (C_F), and thermal volume expansion coefficient (β) are symbols used in the above equations. The control parameters $A_{mush} = 1010$ Pa.s/m^2 and $\lambda_{mush} = 0.001$ were utilized here.

The dynamic viscosity is regarded as dependent on the melt volume fraction (φ), which helps to enhance solver stability and enforce zero velocity in areas that are solid. The viscosity is presented as $\mu_{PCM} = (1\text{-}\varphi)\times\mu_a+\varphi\times\mu_{PCM,l}$, with μ_a being an artificially large viscosity value, set at 10^5 Pa.s. This approach ensures that the viscosity equals the standard dynamic viscosity $\mu_{PCM,l}$ in the liquid region (where $\varphi = 1$) and artificially increases significantly in the solid region (where $\varphi = 0$). The source terms primarily aim to ensure zero velocities in solid areas, and this artificial increase in dynamic viscosity assists in accomplishing this goal. Additionally, this formulation of dynamic viscosity enhances the solver's stability and simplifies simulations without detriment to the physical model.

Eqs. (17a) and (17b) illustrate heat transmission within the MF and PCM phases. The term h_v accounts for the thermal interplay between the two phases of MF and PCM. In these equations, effective thermal conductivities are utilized, as pore structures have a direct impact on thermal conductivities [49]. Here, φ is dependent on the PCM temperature as follows [56]:

$$\varphi(T) = \begin{cases} 0 & T < T_f-\frac{1}{2}\Delta T_f \text{ (Solidous phase)} \\ \frac{(T-T_f)}{\Delta T_f}+\frac{1}{2} & T_f-\frac{1}{2}\Delta T_f \le T \le T_f+\frac{1}{2}\Delta T_f \text{ (Solidous-Liquid region)} \\ 1 & T > T_f+\frac{1}{2}\Delta T_f \text{ (Liquid phase)} \end{cases} \tag{18}$$

Here, ΔT_f represents the phase transition interval surrounding the fusion temperature T_f.

The closure equations for PCM in MF are slightly different from HTF-MF in the previous section since they were involved with forced convection and higher pore Reynolds numbers than natural convection flows in the present section. The uniform permeability (κ) and effective thermal conductivity of MF-PCM ($k_{\text{eff,MF}}$) are calculated using the following formulas [43,49]:

$$k = \frac{(1-\varepsilon)}{3} k_{\text{MF}} \tag{19}$$

while the permeability was computed using Eq. (9) and Frochheimer coefficient using Eq. (12). The volumetric interstitial heat transfer coefficient is employed to assess the heat exchange between the PCM and MF [55]:

$$h_v = \frac{k_{\text{PCM}}}{d_{fs}^2} Nu_v \tag{20}$$

Here, Nu_v refers to the volumetric interstitial heat transfer Nusselt-number [57]. Nu_v is then calculated for low pore scale Reynold numbers as follows [55]:

$$Nu_v = \begin{cases} 76.99 - 152.01\varepsilon + 75.04\varepsilon^2 & 0 \le Re \le 0.1 \\ \left(1.72 + 1.71\varepsilon - 3.46\varepsilon^2\right) Re^{0.26} Pr^{0.28} & 0.1 < Re \le 1 \end{cases} \tag{21}$$

In this context, $\alpha_{\text{PCM}} = k_{\text{PCM}}/(\rho C_p)_{\text{PCM}}$ and $\text{Pr} = \mu_{\text{PCM}}\, \rho_{\text{PCM}}/\alpha_{\text{PCM}}$. The pore scale Reynolds number (Re) is introduced as pore scale Reynolds number, $Re = d_{fs}\, u_{\text{PCM}}\, \rho_{\text{PCM}}/\mu_{\text{PCM}}$.

Various models have been proposed in prior research to calculate the Nusselt number, but a majority of these are tied to high Reynolds number values, usually greater than 1. For free convection of molten PCM within MF, the circulation speeds are quite low, resulting in Reynolds numbers generally below 1. As a result, a specific relationship for Reynolds numbers less than one is needed. The model presented by Yao et al. [55] has been implemented for this purpose. The model of [55] was validated compared to experimental data and showed strong alignment with the PCM's phase transition in MF. The equation is applicable for porosity values between 0.929 and 0.974 and Prandtl numbers between 21 and 41. It is important to highlight that the Nusselt number is non-zero even when velocity is extremely low or at a standstill because thermal diffusion still significantly contributes to the heat transfer between the MF and PCM.

In conclusion, the PCM's effective thermal conductivity was assessed using the following references [43, 49]. To calculate the PCM's properties of the within the mushy area, a linear weight average was employed:

$$k_{\text{eff,PCM}} = k_{\text{PCM}} \frac{\varepsilon + 2}{3} \tag{22a}$$

$$\left(\rho C_p\right)_{\text{PCM}} = \varphi \left(\rho C_p\right)_{\text{s}} + (1-\varphi)\left(\rho C_p\right)_{\text{l}} \tag{22b}$$

$$\rho_{\text{PCM}} = \varphi \rho_{\text{s}} + (1-\varphi)\rho_{\text{l}} \tag{22c}$$

In this case, the s and l subscripts denote the solid and liquid phases. Table 1 provides a summary of the properties of the paraffin, MF, and tube wall.

2.4. Initial and boundary conditions

The heat flux and temperature continuity at all interconnected surfaces were applied as the thermal boundary condition. With respect to LTNE conditions in the MF regions, temperature continuity was first applied. Following this, the heat flux (q) continuity was separated into two components using porosity. As a result, the continuity of heat flux at the intersection of MF and the tube wall was formulated as follows:

$$q_{\text{Wall}} = (1-\varepsilon) q_{\text{PCM}} + \varepsilon q_{\text{MF}} \tag{23}$$

where it is valid for both MF-HTF and MF-PCM domains.

A consistent inlet temperature of T_{h} was employed, with T set at $T_{\text{f}} +$ 15 °C, where T_{f} is the chosen phase change temperature. A steady relative pressure, $p = P_{\text{in}}$, was applied at the HTF inlet boundary.

The outlet was treated with an outflow condition, which includes zero relative pressure and a no heat flux condition, indicated by $-n.q = 0$, where 'n' symbolizes the normal vector to a surface. It was assumed that the shell walls were perfectly insulated, also indicated by $-n.q = 0$. Non-penetrating and No-slip conditions were applied to all walls except for the in and out ports, detailed earlier. The whole LHTES unit was presumed to start at a temperature of $T_{\text{c}} = T_{\text{f}}$-15 °C. A zero-pressure reference point was applied to the lower left corner of the PCM domain.

The continuity of velocity and shear stress were applied for the interface of the foam layer and PCM. Furthermore, the temperature and heat flux continuity was considered at the interface between the porous layer and the clear flow region. The temperature of the MF layer at the interface was assumed to be equal to the temperature of PCM.

However, given the limited temperature variation in this study, the thermophysical properties were assumed to be constant, excluding the PCM, which experiences a phase transition. Moreover, the impact of temperature shifts on density alteration was factored into the buoyancy effect utilizing the Boussinesq approximation in the molten PCM.

2.5. Key parameters

The average quantity of liquefied PCM within the PCM domain (MVF) is described as:

$$MVF = \oint_V \varphi \varepsilon dV \Big/ \oint_V \varepsilon dV \tag{24}$$

Here, dV denotes the volumetric element of the PCM domain. The accumulated thermal energy is calculated as the summation of apparent and latent energies as:

$$\begin{aligned} Q_{sensible} = {} & (\rho C_P)_{\text{MF}} (T - T_0) \oint_V (1-\varepsilon) dV \\ & + \left[\oint_V \left(\int_{T_0}^{T} (\rho C_P)_{\text{PCM}}(T) \varepsilon dT \right) dV \right] \\ & + (\rho C_P)_{\text{Wall}} V_{\text{Wall}} (T - T_0) + (\rho C_P)_{\text{HTF}} V_{\text{HTF}} (T - T_0) \end{aligned} \tag{25}$$

$$Q_{latent} = \varepsilon \oint_V L_{\text{PCM}} \rho_{\text{PCM}} \varphi dV \tag{26}$$

$$Q_{\text{store}} = Q_{\text{latent}} + Q_{\text{sensible}} \tag{27}$$

Energy Storage Power is computed as.

Table 1
A Summary of the thermophysical characteristics for involved material.

Materials	ρ (kg/m^3)	k (W/m.K)	C_p (J/kg.K)	L (kJ/kg)	T_m (°C)	μ (kg/m.s)	β (1/K)
Paraffin (solid/liquid) [58–60]	916/790	0.21/0.12	2700/2900	176	49–54*	0.0036	0.00091
Water [61]	997.1	0.613	4179	–	–	0.000957	0.00021
Copper foam [62]	8900	380	386	–	–	–	–

* $T_{\text{f}} = 51.5$.

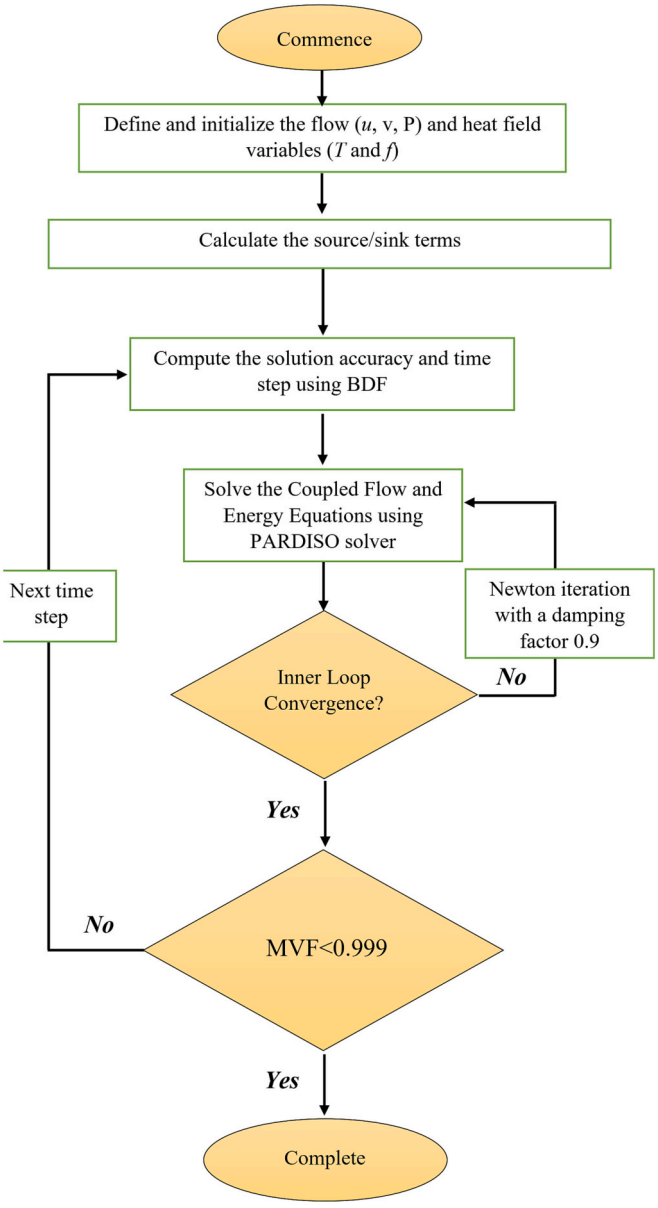

Fig. 4. A graphical representation of the FEM procedure for simulating the storage of thermal energy *via* latent heat in the shell-tube storage unit.

$$Power = Q_{store}/t \tag{28}$$

Power signifies the average power of TES.

3. Numerical method, mesh study, and model verification

3.1. Finite element method

This study utilizes the finite element method (FEM) to solve the partial differential equations presented in Eqs. (1), (2–6), and (15)–(17), along with the initial and boundary conditions. The momentum and heat equations were transformed into a weak form and solved using a second-order dissertation. The equations were integrated over elements using Gauss quadrature integration, resulting in an algebraic set of residual equations. These residual equations were solved iteratively with the PARDISO solver, utilizing the Newton method in a coupled manner. A damping factor of 0.9 was employed to increase convergence. The time step was regulated using the backward differential formula with a free order ranging from 1 to 2. The solution method is illustrated in Fig. 4.

Table 2
Mesh details and computational time for charging (melting) and discharging (solidification) process.

N	Quads	Computational time (min)	
		Charging	Discharging
2	6660	71	51
3	15,232	166	124
4	26,969	337	245
5	42,036	534	406
6	60,433	822	604

3.2. Mesh study

A mesh study is an essential phase in numerical simulations to guarantee the precision and dependability of the outcomes. A mesh, which in this case consists of connected quads to represent the problem's geometry, is a discretization of the computing domain. The simulation's convergence, the correctness of the solutions, and computational time are all directly impacted by the mesh size. Mesh study examines how different mesh sizes affect simulation results in order to choose a mesh resolution that strikes a compromise between accuracy and computing effectiveness. For various mesh resolutions, Table 2 shows the mesh information and computation time for the charging (melting) and discharging (solidification) processes. The number of quads and corresponding computation durations are shown in the table for $N = 2, 3, 4, 5$, and 6 different mesh refinement levels.

The number of quads grows as the mesh is fine-tuned (N is raised), producing increasingly accurate representations of the geometry. Longer computation durations for the charging and draining operations are a side effect of this improvement. For instance, when N is increased from 2 to 6, the number of quads grows from 6660 to 60,433, and the computational times for charging and discharging both jump from 71 to 822 min. The effect of mesh size on the *MVF* accuracy is shown in Fig. 5. As seen, adding adopted mesh provides acceptable accuracy for most engineering applications. However, a low-resolution mesh impacts the solution convergence.

This mesh resolution was selected based on the mesh study findings (Table 2 and Fig. 5) and considering the trade-off between MVF accuracy and computational time. For both the charging and discharging processes, the mesh with $N = 4$ maintains a tolerable computing time while providing a sufficiently accurate representation of the geometry. A view of the chosen mesh with $N = 4$ for calculations is shown in Fig. 6. The

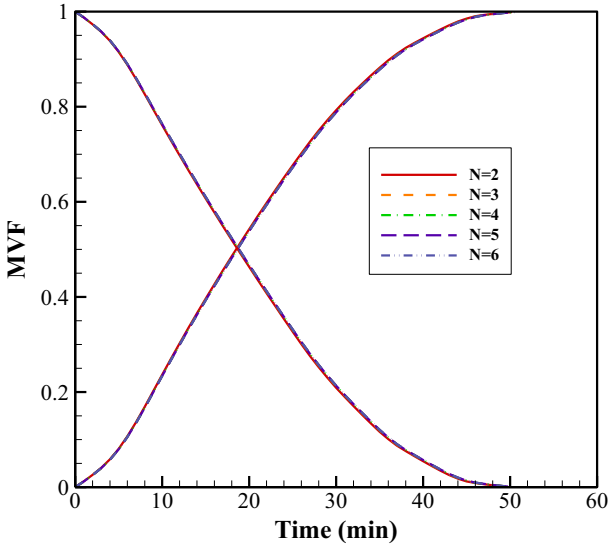

Fig. 5. Impact of mesh size on the *MVF* accuracy.

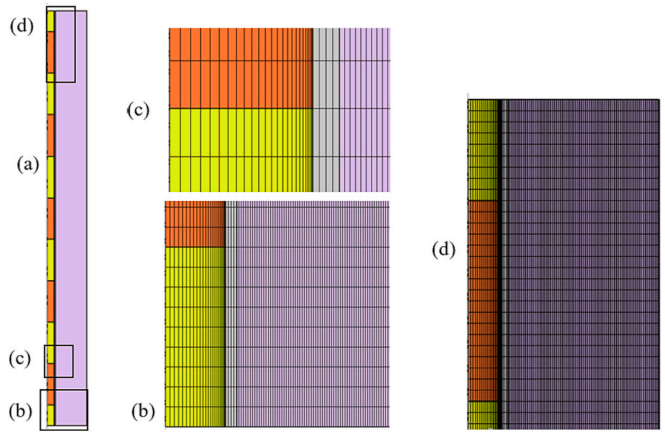

Fig. 6. A view of the selected mesh with $N = 4$ for computations.

mesh at HTF size, MF layer, and wall are depicted in detail. It should be noted that the mesh at the HTF tube is non-uniform and is denser close to the tube surface. The mesh has been stretched with a stretching factor of 10.

3.3. Model verification

The research of Zheng et al. [62], which experimentally captured the melting interface in MFs, was utilized to confirm the simulated findings produced in this study. The simulation was done on a 10 cm by 10 cm square of uniformly porous MF with a porosity of 97.5 %. At the bottom of the enclosure, a heat source was supplied, and the actual melting interface of copper foam-paraffin was compared to the simulation data. The findings shown in Fig. 7 are in excellent accordance with the experimental pictures.

To test the model's and code's correctness, experimental data reported by Kamkari et al. in their work on melting lauric acid PCM inside a 120 × 50 mm enclosure were compared to the model and code. In this investigation, the same model was simulated, and the resultant MVF was compared to theoretical and experimental data from the literature. It was determined that the simulated and present data were in excellent agreement, verifying the accuracy of the calculations and the model, as illustrated in Fig. 8.

4. Results and discussions

This section aims to investigate the impact of MF layers placed in the HTF tube on the charging and discharging behavior of a shell-tube shape LHTES unit. Here, three inlet gauge pressures of $P_{in} = 250$ Pa, 500 Pa, and 750 Pa were investigated.

Table 3 presents the results of an investigation into the phase change times at various inlet pressures for an LHTES unit. The study is focused on six distinct cases (A-F), as depicted in Fig. 3, each featuring a different distribution and concentration of MF (MF) within the unit.

Cases A to C each contain 50 % MF but with varying distributions of the MF within the unit. Although these cases share the same amount of MF, the differences in distribution are expected to influence the phase change times. In contrast, Cases D, E, and F feature MF layers placed at the center of the HTF tube, with decreasing amounts of MF in each case. Case D contains 25 % MF, while Cases E and F contain 12.5 % and 6.25 % MF, respectively. Table 3 displays the melting and solidification times for each case under three inlet pressures: 250 Pa, 500 Pa, and 750 Pa. A comparison of the results for the six cases reveals several key findings and trends:

Melting times generally decrease with increasing inlet pressure

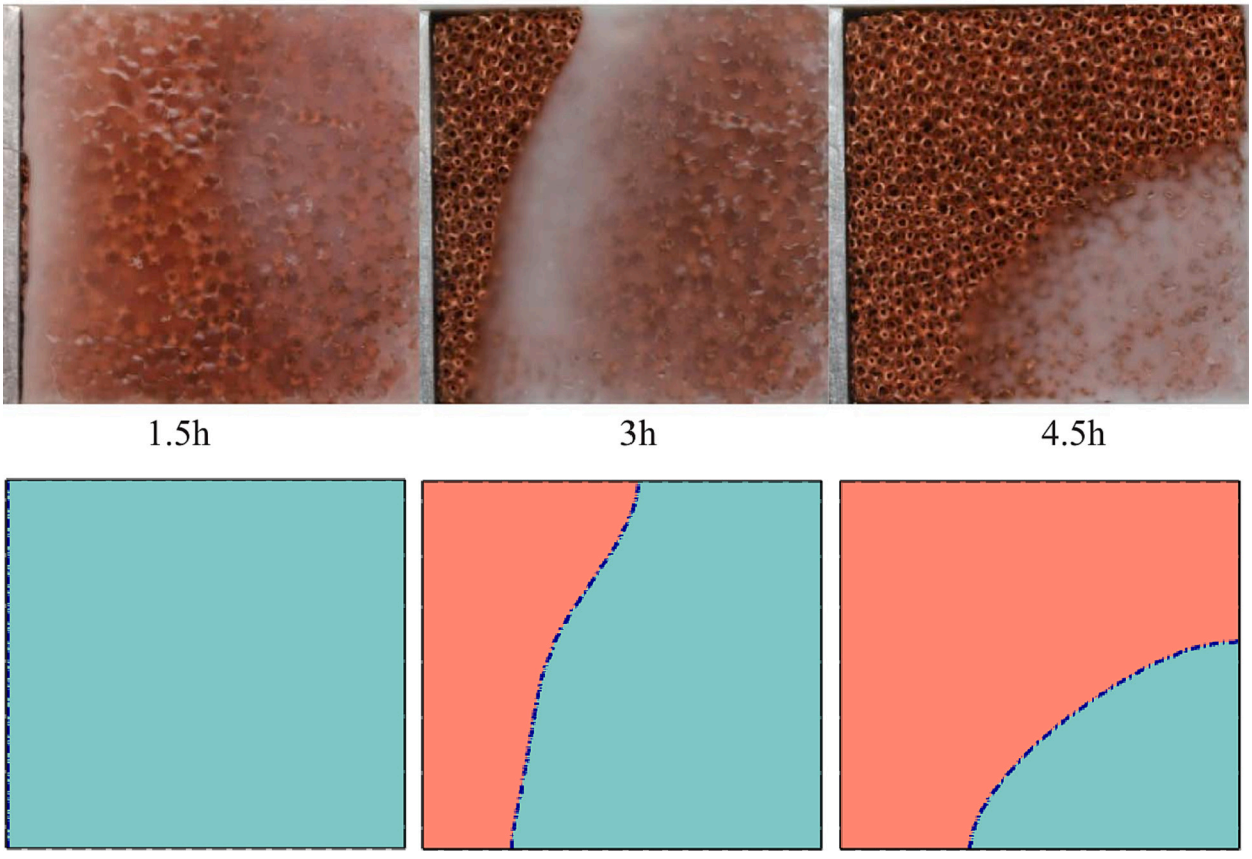

Fig. 7. The melting interfaces of paraffin wax in copper foam, as observed in the physical experiment by Zheng et al. [62], and as simulated in the current study.

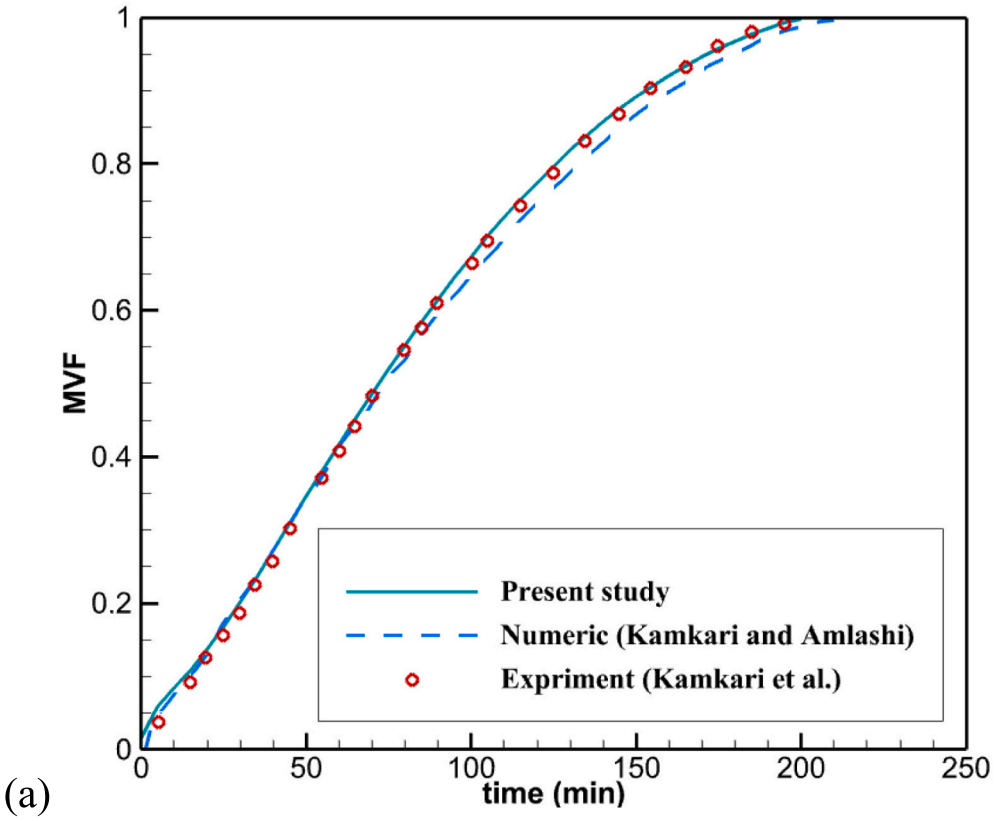

(a)

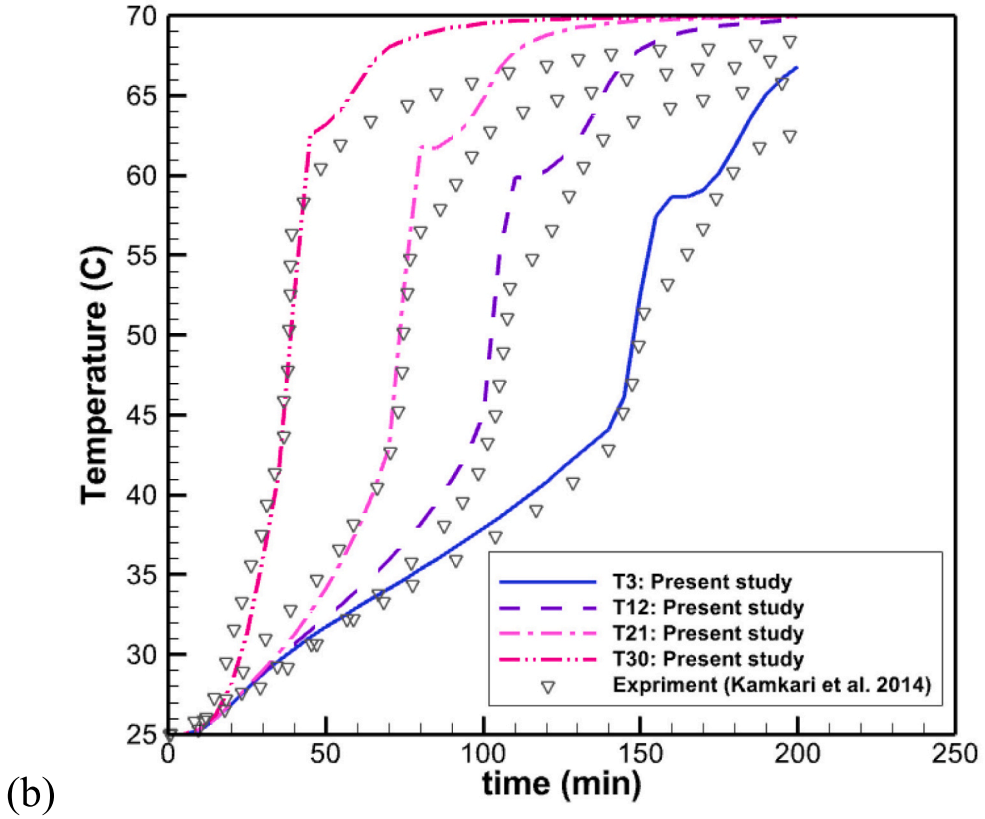

(b)

Fig. 8. A comparison of MVF and temperature distribution in a cavity during the phase change with the empirical and theoretical literature studies [63,64].

Table 3
Phase change time at various inlet pressures for a LHTES unit.

	Melting time (Min)			Solidification (Min)		
Inlet Pressure	250 Pa	500 Pa	750 Pa	250 Pa	500 Pa	750 Pa
Case A	65.2	47.0	40.6	64.1	46.2	40.0
Case B	68.9	50.4	43.8	67.6	49.9	43.1
Case C	93.0	72.2	64.1	91.0	70.9	63.3
Case D	85.5	70.6	64.2	83.7	69.8	63.3
Case E	75.3	64.2	59.2	74.3	63.1	58.1
Case F	66.2	57.7	53.8	65.3	56.3	52.9

across all cases. This consistent trend indicates that higher inlet pressures enhance the melting process, reducing the time required for the phase change to occur. The most significant decrease in melting time is observed between the 250 Pa and 500 Pa inlet pressures, while the difference between the 500 Pa and 750 Pa pressures is less pronounced.

Cases with a higher MF concentration (Cases A-C) generally have shorter melting times compared to Cases D—F, which have a lower MF concentration. This suggests that a higher MF concentration leads to more efficient melting, possibly due to the increased thermal conductivity and lower thermal resistance at the HTF side provided by the MF. However, the distribution of MF also plays a role, as evidenced by the varying melting times for Cases A, B, and C, despite their identical MF concentrations.

The distribution of MF impacts both the melting and solidification times. Cases A, B, and C have different distributions of 50 % MF, and their melting and solidification times show noticeable variations. Among these cases, Case C has the longest melting and solidification times, suggesting that its MF distribution is the least effective at facilitating the phase change processes.

For Cases D, E, and F, where the MF layer is positioned at the center of the HTF tube, the decreasing MF concentration from Case D to Case F results in progressively shorter melting times. This trend indicates that a lower MF concentration in the central layer may lead to more efficient melting under the given conditions. As the amount of the MF layer reduces, the flow resistance decreases, and since the inlet pressure is fixed, the HTF flow rate increases.

Similar to the melting times, solidification times generally decrease with increasing inlet pressure for all cases. The most significant decrease in solidification time is observed between the 250 Pa and 500 Pa inlet pressures, with a smaller difference between the 500 Pa and 750 Pa pressures. The solidification times for Cases A, B, and C show variations, further emphasizing the influence of MF distribution on the phase transition process. Cases D, E, and F, with their central MF layers, display a trend of decreasing solidification times as the MF concentration is reduced, mirroring the trend observed in the melting times for these cases. This suggests that a centralized MF layer with lower concentrations may be more effective in facilitating phase change processes under the given conditions.

Table 4 summarizes the tube Reynolds number (Re_{HTF}) for various cases (A-F) and inlet pressure differences (250 Pa, 500 Pa, and 750 Pa). The properties of water are constant (as reported in Table 1), and thus, the Reynolds number is controlled by the average HTF tube velocity outlet.

Table 4 shows Reynolds numbers vary widely across the different cases, as well as with changing inlet pressure differences. The results reveal a clear trend of increasing Reynolds numbers with increasing inlet pressure differences for each case. Cases A, B, and C demonstrate similar Reynolds numbers for each inlet pressure difference. For these cases, at 250 Pa inlet pressure, the Reynolds number is 197, which remains constant for both Case A and Case B. As the inlet pressure rises to 500 Pa, the Reynolds number increases to 354 for both cases. At 750 Pa, the Reynolds number for Case A and Case B remains the same at 489. Case C exhibits a slightly different behavior, with the Reynolds number at 355 for an inlet pressure of 500 Pa while maintaining the same values as Case A and B for the other two inlet pressures. Since, in these cases, the amount of MF layer is fixed, the distribution of the layer induces minimal impact on the pressure drop.

Table 4
Tube Reynolds number (Re_{HTF}) for various cases and inlet pressure differences.

Inlet Pressure	250 Pa	500 Pa	750 Pa
Case A	197	354	489
Case B	197	354	489
Case C	197	355	489
Case D	353	607	817
Case E	604	995	1308
Case F	987	1567	2024

In comparison, cases D, E, and F demonstrate a more pronounced increase in Reynolds numbers with rising inlet pressure differences. For Case D, the Reynolds number starts at 353 at 250 Pa, then increases to 607 at 500 Pa, and finally reaches 817 at 750 Pa. Case E experiences a more dramatic increase, with the Reynolds number beginning at 604 at 250 Pa, jumping to 995 at 500 Pa, and reaching 1308 at 750 Pa. Case F exhibits the most substantial increase in Reynolds numbers, with values of 987, 1567, and 2024 for inlet pressures of 250 Pa, 500 Pa, and 750 Pa, respectively. Since in Cases D—F, the amount of MF layer reduces, the resistance to the fluid flow also drops, and thus, larger outlet velocity fluctuations (Re_{HTF}) can be seen as the inlet pressure changes.

Fig. 9 illustrates the temporal progression of melting and solidification for Cases A-F under an inlet pressure of 250 Pa. The findings reveal that Cases A and F yield the quickest charging and discharging time history compared to the other cases examined. Intriguingly, Case A comprises a 50 % MF layer, while Case F contains only a 6.5 % MF layer.

The reasons behind this behavior can be ascribed to the MF layer's resistance to fluid flow. Given that a fixed inlet pressure was employed as a boundary condition, an MF layer can diminish fluid flow, suppressing convective heat transfer. Nevertheless, the MF layer also enhances the heat transfer rate by improving the overall thermal conductivity and amplifying the heat transfer surface at the pore level. Conversely, a thin MF layer (Case F) imposes minimal resistance against fluid flow, resulting in a higher flow rate within the HTF tube. Thus, a high flow rate contributes to an elevated overall heat transfer rate.

Conversely, a substantially thick layer of MF, when optimally distributed, significantly enhances the conduction of heat transfer on the HTF side. However, this also results in a pronounced pressure drop in the fluid flow, subsequently lowering the flow rate. A decrease in flow rate can potentially diminish the overall heat transfer efficiency. Consequently, both scenarios - a thin MF layer (Case F) and an optimally distributed, thick MF layer – (Case A) present themselves as feasible options for enhancing heat transfer.

Case A, characterized by a lower flow rate, might result in a higher HTF outlet temperature compared to Case F. Therefore, the selection between these two design scenarios would depend on the specific objectives of the storage design. Both designs could be of practical significance, each with its unique advantages based on the overarching storage goals.

Fig. 10 contrasts the melting and solidification profiles of the metal volume fraction (MVF) for various inlet pressures in Cases A and F. Both cases exhibit nearly identical MVF time histories at a low inlet pressure of 250 Pa. However, Case A demonstrates more rapid melting and solidification behavior as the inlet pressure rises. The increase in inlet pressure elevates the flow rate within the MF layer and heightens the temperature difference between the MF and HTF.

Consequently, a higher flow rate amplifies the thermal interaction with the MF layer and the MF layer's thermal conductivity in heat transfer. As Fig. 10 displays, increasing the inlet pressure accelerates the phase change within the system. Conversely, in Case F, where only a small amount of MF is present, an increase in inlet pressure further augments the flow rate within the HTF tube. However, the flow rate is already high in this situation, and there is a significant temperature

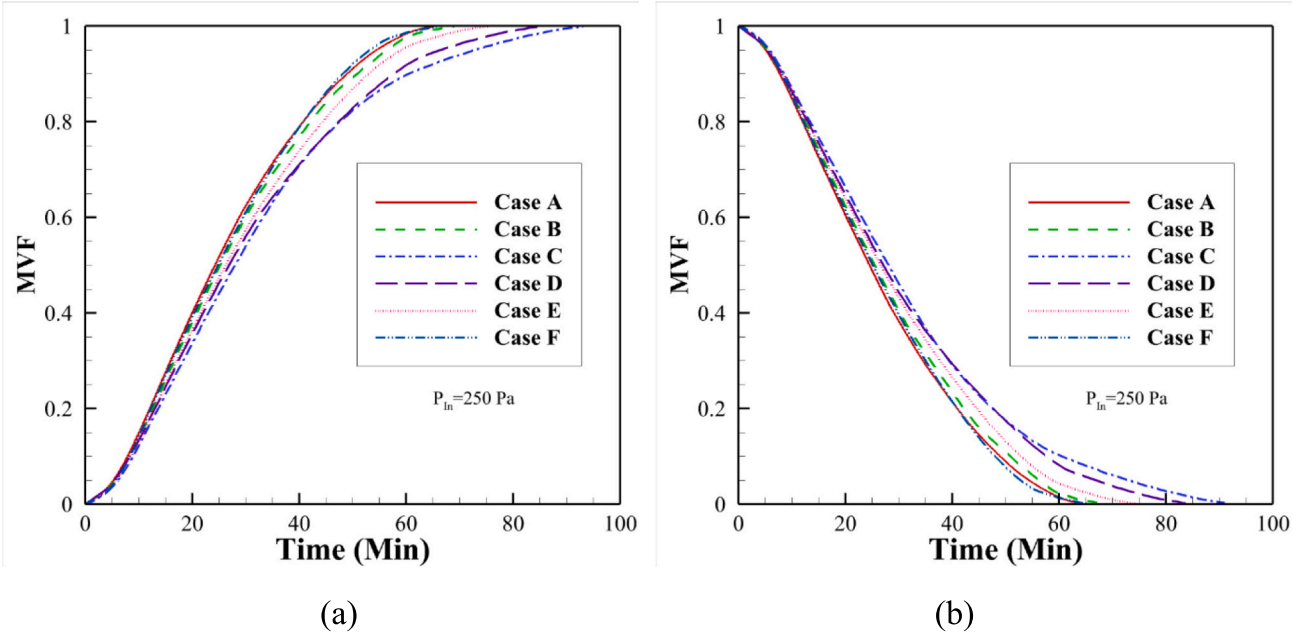

Fig. 9. Time history of MVF when the inlet pressure is 250 Pa during (a) melting, and (b) solidification.

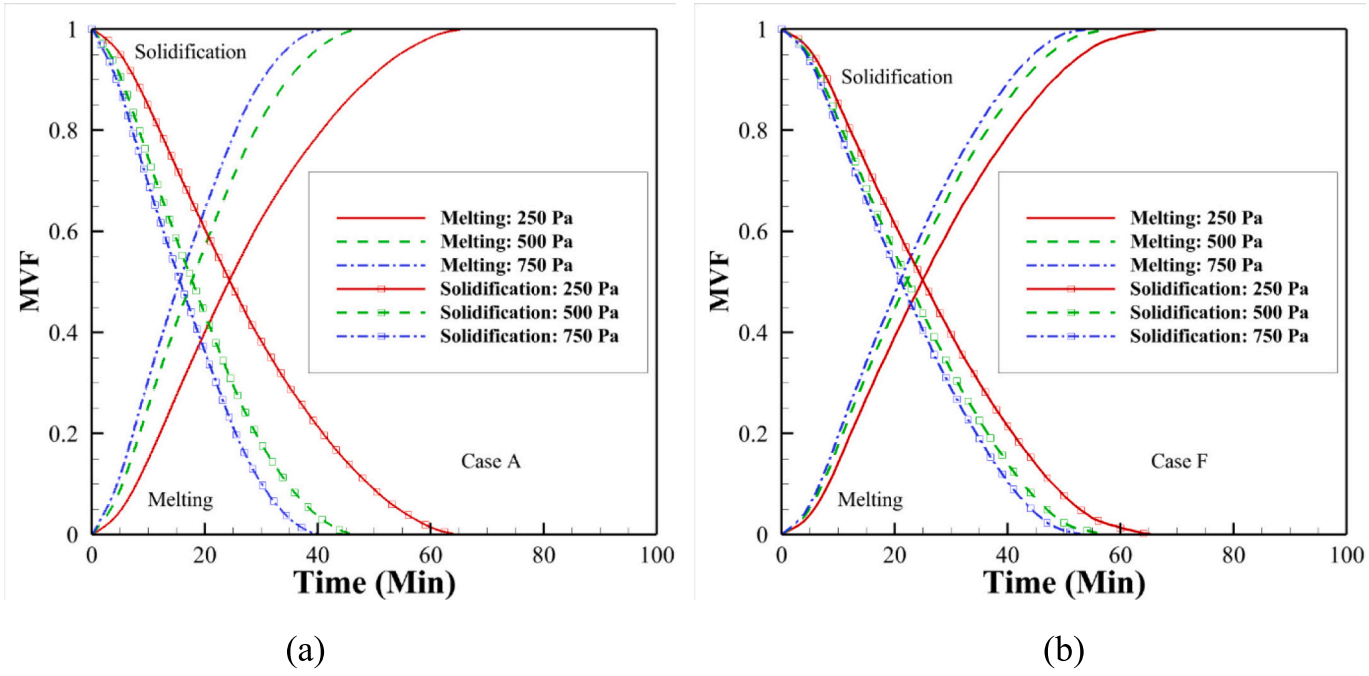

Fig. 10. Time history of MVF for various inlet pressures (a) Case A, (b) Case F.

difference between the tube wall and the HTF. In this case, a further increase in the flow rate does not improve the heat transfer rate.

Fig. 11 illustrates the accumulated and released heat in the LHTES unit during the melting and solidification. The outcomes presented in this figure correspond well with the metal volume fraction (MVF) time history results discussed in Figs. 9 and 10. This correlation can be attributed to the fact that most heat transfer occurs in the form of latent heat, which is directly associated with MVF.

Among the cases examined, Case A offers the most rapid thermal energy storage and release, followed closely by Case F. This observation highlights the effectiveness of Case A in terms of both energy storage and retrieval, owing to its unique combination of MF layer properties and inlet pressure. The results suggest that the optimal design of LHTES systems should consider factors such as MF layer composition and inlet pressure to ensure efficient heat transfer and energy storage/release performance.

It is crucial to highlight that both melting and solidification cases exhibit nearly identical durations for the phase change process. However, these times are not perfectly identical, a discrepancy that can be ascribed to the role of the convection heat transfer mechanism. During the melting phase, the molten region initiates adjacent to the heated tube, progressively extending through the solid area. In this stage, the impact of the convection heat transfer is initially minimal, but as the molten region expands, the role of convection becomes more significant.

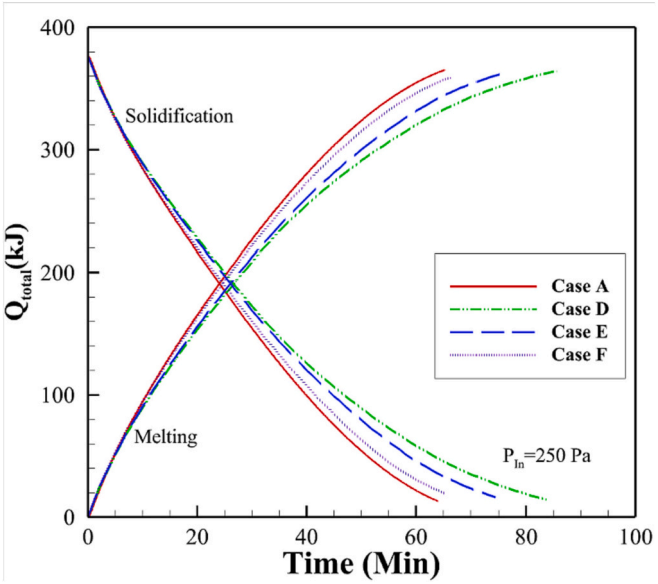

Fig. 11. Time history of total stored energy for various cases when inlet pressure is 250 Pa.

On the contrary, the solidification process begins at the tube wall. At this point, the entire storage unit is in a molten state, creating a robust convection heat transfer mechanism. As the solidification progresses, the solid layer's thickness over the tube wall increases, introducing a conduction resistance to heat transfer, and the molten region subsequently decreases. Therefore, this inverse process involves a different heat transfer mechanism compared to the melting phase. Thus, due to these differing heat transfer dynamics during melting and solidification, the overall durations of these two processes do not precisely match.

Fig. 12 presents the melting region and streamlines for three Cases: A, C, and F. Meanwhile, Fig. 13 depicts the temperature contours of the temperature difference (T-$T_{initial}$) during the melting process for the same cases as in Fig. 12, as well as the temperature difference on the HTF side. These images are provided at 10-min intervals.

In Case A, Fig. 12 reveals that melting begins at the bottom and gradually develops upwards. Observing Fig. 13, it becomes apparent that the temperature difference at the inlet is quite high, and the presence of an MF layer serves to enhance the heat transfer rate. Consequently, in Case A, the most significant heat transfer on the HTF side occurs at the bottom area. As time progresses, PCM at the enclosure's bottom melts, causing the melting interface to move away from the HTF tube. This results in increased heat transfer resistance on the PCM side in the bottom area, reducing heat transfer at the bottom. Thus, the HTF liquid reaches the middle of the HTF tube at a higher temperature.

The MF layer in the middle section aids in heat transfer and conveys heat to the PCM domain in the central areas of the chamber. This facilitates the development of liquid PCM regions in the middle and top sections of the PCM chamber. The heated liquid PCM at the bottom region also circulates toward the top regions due to natural convection flows, further melting the top region. Examining the color maps, it becomes evident that the HTF outlet temperature difference is approximately 15 °C at the initial time ($t = 10$ mins), increasing to 17 °C, 19 °C, 21 °C, and 23 °C at 20, 30, and 40 min of charging time. A low-temperature difference shows a larger temperature drop compared to the inlet temperature. As demonstrated, Case A provides an excellent temperature drop during the charging process, making it an ideal design for applications that aim to directly charge or discharge an LHTES unit at low flow rates.

In Case C, the MF layer is positioned around the center of the HTF tube. In this configuration, the heat transfer rate is high at the inlet as the fresh HTF liquid enters the tube and in the middle due to the presence of

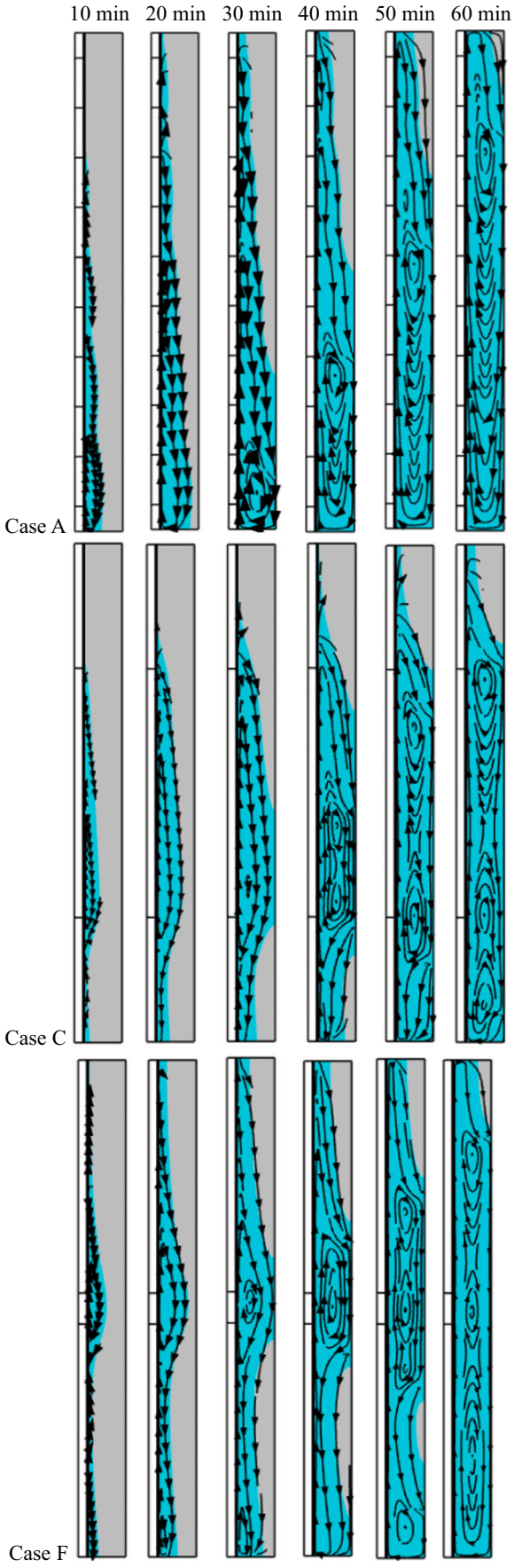

Fig. 12. The time history of melting process for three Cases A, C, and F.

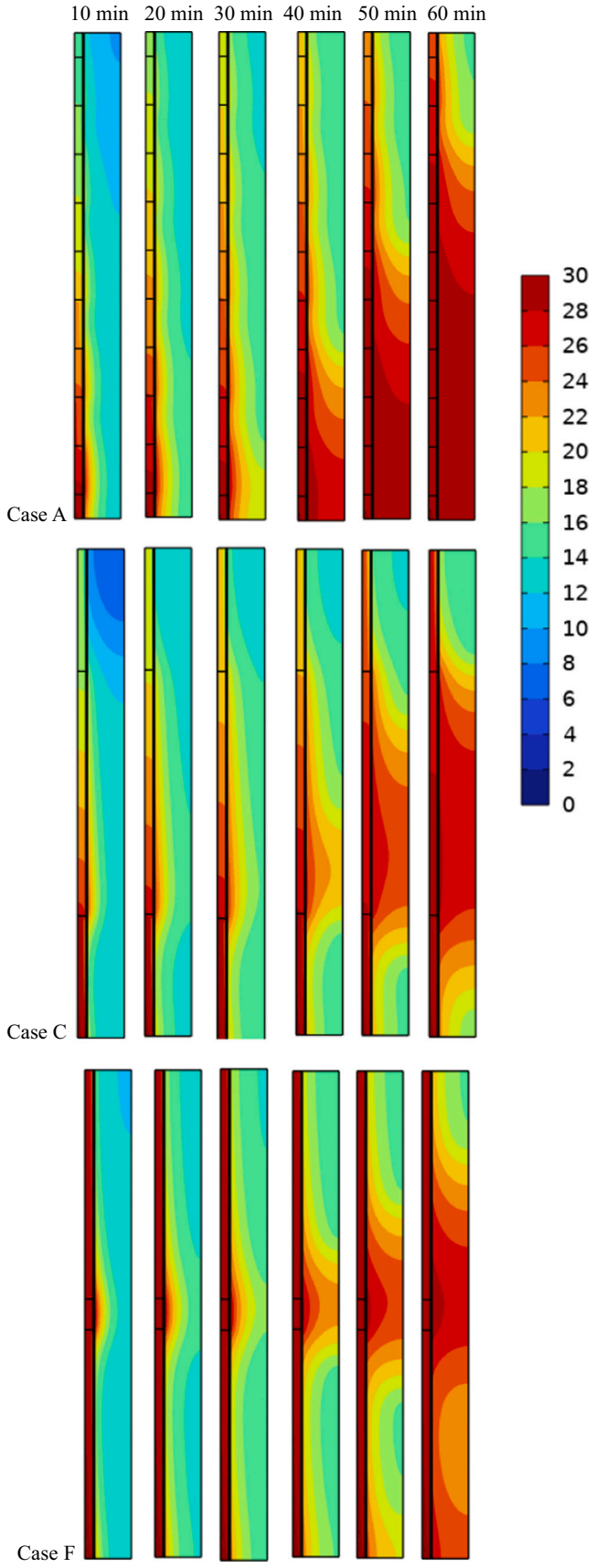

Fig. 13. The time history of temperature contours (T-$T_{initial}$) °C during the melting process for three Cases A, C, and F.

the thermally conductive MF layer. The melting pattern reveals a slight liquid region at the bottom and a more pronounced region in the middle of the PCM chamber. Interestingly, the middle region first expands toward the bottom (40 mins) and then upwards. The top region remains the last solid portion of the PCM chamber after 60 min of melting.

Examining the temperature contours reveals a favorable temperature drop compared to the inlet temperature during the initial and middle melting times (t = 10–40 min). However, as time progresses, the outlet temperature approaches the inlet temperature, indicating a reduced thermal charging rate in the later stages of the process.

Case F features a small layer of MF at the center. Melting initiates in a minor region in the middle where the MF layer is located, as well as at the bottom where the heat transfer rate at the tube wall is high. The melting region expands into the PCM chamber from both the center and bottom. The streamlines exhibit effective natural convection circulation within the molten area. A modest temperature drop is observed at the HTF tube outlet during the initial times when energy storage is substantial. However, the temperature drop decreases as time progresses. The low-temperature drop at the outlet in Case F can be attributed to the high flow rate. Essentially, the absorbed heat by the PCM chamber is insufficient to raise the temperature of the large volume of the following liquid in the HTF tube. As a result, this design may be more suitable for applications that incorporate an HTF storage tank and an internal circulating loop, which can gradually inject heat into the storage unit. This approach can help to maintain a balance between the heat absorption capacity of the PCM chamber and the heat transfer capabilities of the HTF system.

5. Conclusions

The current research investigates the impact of various MF layer configurations on the heat transfer fluid inside a shell-tube LHTES system. In the study, six distinct cases (Case A-F) were considered, representing different percentages of MF coverage and varied MF layer dimensions. The configurations directly impact heat transfer characteristics, flow distribution, pressure drops, and flow resistance. Higher MF coverage typically leads to enhanced heat transfer and more uniform flow distribution but may also introduce higher pressure drops and flow resistance. The FEM solved the partial differential equations. The impact of inlet pressure and MF configuration was addressed on the melting and solidification process. The main findings of the study can be listed as follows:

- The study investigates the impact of MF layers in a shell-tube LHTES unit under varying inlet pressures (250 Pa, 500 Pa, and 750 Pa) and MF distributions and concentrations (Cases A-F). The results indicate that higher inlet pressures generally lead to faster melting and solidification times, with the most significant decrease in phase change time observed between 250 Pa and 500 Pa inlet pressures. The variations in melting and solidification times for the six cases highlight the importance of both MF concentration and distribution in the LHTES unit.
- Cases A to C, with a 50 % MF concentration and varying distributions, exhibit shorter melting times than Cases D to F, which have decreasing MF concentrations. This suggests that a higher MF concentration enhances the melting process due to increased thermal conductivity and lower thermal resistance at the HTF side. The melting and solidification times for Cases A, B, and C show noticeable variations, emphasizing the impact of MF distribution on phase change processes.
- For Cases D, E, and F, where the MF layer is located at the center of the HTF tube, and the MF concentration decreases from 25 % to 6.25 %, the melting times progressively decrease. This trend suggests a lower MF concentration in the central layer leads to more efficient melting under the given conditions. The reduced MF layer results in

decreased flow resistance, and since the inlet pressure is fixed, the HTF flow rate increases.

- Similar to melting times, solidification times generally decrease with increasing inlet pressures for all cases. The variations in solidification times for Cases A, B, and C further emphasize the impact of MF distribution on phase change processes. Cases D, E, and F display decreasing solidification times as the MF concentration is reduced, mirroring the trend observed in the melting times. This indicates that a centralized MF layer with lower concentrations may be more effective in facilitating phase change processes under the given conditions.
- Cases A, B, and C demonstrate similar Reynolds numbers for each inlet pressure difference, with minimal impact on the pressure drop due to the fixed amount of MF layer. In contrast, Cases D, E, and F exhibit a more pronounced increase in Reynolds numbers with rising inlet pressure differences as the amount of MF layer reduces and the resistance to fluid flow drops.
- Cases A and F exhibit the quickest charging and discharging time history among the cases examined. Case A has a 50 % MF layer, while Case F has only a 6.5 % MF layer. The behavior can be attributed to the MF layer's resistance to fluid flow. In Case A, the MF layer enhances the heat transfer rate by improving overall thermal conductivity and amplifying the heat transfer surface at the pore level. In Case F, a thin MF layer imposes minimal resistance against fluid flow, resulting in a higher flow rate within the HTF tube and an elevated overall heat transfer rate.
- The findings suggest that the optimal design of LHTES systems should consider factors such as MF layer composition and inlet pressure to ensure efficient heat transfer and energy storage/release performance. Case A offers the most rapid thermal energy storage and release, followed closely by Case F. The effectiveness of these cases can be attributed to their unique combination of MF layer properties and inlet pressure.

CRediT authorship contribution statement

Mehdi Ghalambaz: Conceptualization, Methodology, Formal analysis, Data Curation, Writing - Review & Editing, Conceptualization, Investigation, Software, Validation **Mikhail Sheremet:** Visualization, Original draft preparation, Investigation, Formal analysis, Data Curation. **Zehba Raizah:** Investigation. Formal analysis, Writing - Review & Editing, Conceptualization, Investigation. **Nevzat Akkurt:** Conceptualization, Investigation, Writing - Review & Editing. **M. Ghalambaz:** Methodology, Conceptualization, Investigation, Formal analysis, Data Curation, Writing - Review & Editing, Supervision.

Declaration of competing interest

The authors clarify that there is no conflict of interest for report.

Data availability

No data was used for the research described in the article.

Acknowledgments

The authors extend their appreciation to the Deanship of Scientific Research at King Khalid University, Abha, Saudi Arabia, for funding this work through the Research Group Project under Grant Number (RGP.1/505/44). The study of Mikhail Sheremet and Mohammad Ghalambaz was supported by the Tomsk State University Development Programme (Priority-2030).

References

[1] R. Yang, D. Li, M. Arıcı, B. Wang, Y. Wu, Y. Ma, X. Yang, Photothermal performance of plastic greenhouse embedded with phase change materials in translucent envelopes: a dynamic experimental study, J. Energy Storage 58 (2023), 106375.
[2] S. Kalaiselvam, R. Parameshwaran, Thermal Energy Storage Technologies for Sustainability: Systems Design, Assessment and Applications, Elsevier, 2014.
[3] R. Elarem, T. Alqahtani, S. Mellouli, G.A. El Awadi, S. Algarni, L. Kolsi, Experimental investigations on thermophysical properties of nano-enhanced phase change materials for thermal energy storage applications, Alex. Eng. J. 61 (9) (2022) 7037–7044.
[4] F. Hassan, F. Jamil, A. Hussain, H.M. Ali, M.M. Janjua, S. Khushnood, M. Farhan, K. Altaf, Z. Said, C. Li, Recent advancements in latent heat phase change materials and their applications for thermal energy storage and buildings: a state of the art review, Sustain. Energy Technol. Assess. 49 (2022), 101646.
[5] F. Agyenim, N. Hewitt, P. Eames, M. Smyth, A review of materials, heat transfer and phase change problem formulation for latent heat thermal energy storage systems (LHTESS), Renew. Sust. Energ. Rev. 14 (2) (2010) 615–628.
[6] A. Jodeiri, M. Goldsworthy, S. Buffa, M. Cozzini, Role of sustainable heat sources in transition towards fourth generation district heating–a review, Renew. Sust. Energ. Rev. 158 (2022), 112156.
[7] H. Lund, B. Möller, B.V. Mathiesen, A. Dyrelund, The role of district heating in future renewable energy systems, Energy 35 (3) (2010) 1381–1390.
[8] R. Naveenkumar, M. Ravichandran, V. Mohanavel, A. Karthick, L.S.R.L. Aswin, S.S. H. Priyanka, S.K. Kumar, S.P. Kumar, Review on phase change materials for solar energy storage applications, Environ. Sci. Pollut. Res. 29 (7) (2022) 9491–9532.
[9] C. Xu, H. Zhang, G. Fang, Review on thermal conductivity improvement of phase change materials with enhanced additives for thermal energy storage, J. Energy Storage 51 (2022), 104568.
[10] S. Shoeibi, H. Kargarsharifabad, S.A.A. Mirjalily, M. Sadi, A. Arabkoohsar, A comprehensive review of nano-enhanced phase change materials on solar energy applications, J. Energy Storage 50 (2022), 104262.
[11] A. Khademi, S.A. Abtahi Mehrjardi, Z. Said, A.J. Chamkha, Heat transfer improvement in a thermal energy storage system using auxiliary fluid instead of nano-PCM in an inclined enclosure: a comparative study, J. Appl. Comput. Mech. 9 (2) (2023) 475–486.
[12] M. Ghalambaz, M. Aljaghtham, A.J. Chamkha, A. Abdullah, U. Alqsair, M. Ghalambaz, Dynamic melting in an open enclosure supported by a partial layer of metal foam: a fast thermal charging approach, Int. J. Heat Mass Transf. 203 (2023), 123760.
[13] M. Ghalambaz, H. Jin, A. Bagheri, O. Younis, D. Wen, Convective flow and heat transfer of nano-encapsulated phase change material (NEPCM) dispersions along a vertical surface, Facta Universitatis Ser. Mech. Eng. 20 (3) (2022) 519–538.
[14] H. Peng, J. Wang, X. Zhang, J. Ma, T. Shen, S. Li, B. Dong, A review on synthesis, characterization and application of nanoencapsulated phase change materials for thermal energy storage systems, Appl. Therm. Eng. 185 (2021), 116326.
[15] M. Aramesh, B. Shabani, Metal foams application to enhance the thermal performance of phase change materials: a review of experimental studies to understand the mechanisms, J. Energy Storage 50 (2022), 104650.
[16] C. Zhao, M. Opolot, M. Liu, J. Wang, F. Bruno, S. Mancin, K. Hooman, Review of analytical studies of melting rate enhancement with fin and/or foam inserts, Appl. Therm. Eng. 207 (2022), 118154.
[17] W. Cui, T. Si, X. Li, X. Li, L. Lu, T. Ma, Q. Wang, Heat transfer enhancement of phase change materials embedded with metal foam for thermal energy storage: a review, Renew. Sust. Energ. Rev. 169 (2022), 112912.
[18] K. Boomsma, D. Poulikakos, F. Zwick, Metal foams as compact high performance heat exchangers, Mech. Mater. 35 (12) (2003) 1161–1176.
[19] H. Ji, D.P. Sellan, M.T. Pettes, X. Kong, J. Ji, L. Shi, R.S. Ruoff, Enhanced thermal conductivity of phase change materials with ultrathin-graphite foams for thermal energy storage, Energy Environ. Sci. 7 (3) (2014) 1185–1192.
[20] J. Xu, X. Zhang, L. Zou, A review: Progress and perspectives of research on the functionalities of phase change materials, J. Energy Storage 54 (2022), 105341.
[21] K. Du, J. Calautit, P. Eames, Y. Wu, A state-of-the-art review of the application of phase change materials (PCM) in mobilized-thermal energy storage (M-TES) for recovering low-temperature industrial waste heat (IWH) for distributed heat supply, Renew. Energy 168 (2021) 1040–1057.
[22] F.K. Malik, M.M. Khan, H.F. Ahmed, M. Irfan, I.U. Ahad, Performance characteristics of PCM based thermal energy storage system for fluctuating waste heat sources, Case Stud. Therm. Eng. 34 (2022), 102012.
[23] W. Liu, Y. Bie, T. Xu, A. Cichon, G. Krolczyk, Z. Li, Heat transfer enhancement of latent heat thermal energy storage in solar heating system: a state-of-the-art review, J. Energy Storage 46 (2022), 103727.
[24] R.K. Shah, D.P. Sekulic, Fundamentals of Heat Exchanger Design, John Wiley & Sons, 2003.
[25] A. Chibani, S. Merouani, F. Benmoussa, Computational analysis of the melting process of phase change material-metal foam-based latent thermal energy storage unit: the heat exchanger configuration, J. Energy Storage 42 (2021), 103071.
[26] P.K. Tamkhade, R.D. Lande, R.B. Gurav, M.M. Lele, Investigations on tube in tube metal foam heat exchanger, Mater. Today Proc. 72 (2023) 951–957.
[27] P.T. Sardari, D. Giddings, D. Grant, M. Gillott, G.S. Walker, Discharge of a composite metal foam/phase change material to air heat exchanger for a domestic thermal storage unit, Renew. Energy 148 (2020) 987–1001.
[28] J. Guo, Z. Du, G. Liu, X. Yang, M.-J. Li, Compression effect of metal foam on melting phase change in a shell-and-tube unit, Appl. Therm. Eng. 206 (2022), 118124.

[29] P. Talebizadehsardari, H.I. Mohammed, J.M. Mahdi, M. Gillott, G.S. Walker, D. Grant, D. Giddings, Effect of airflow channel arrangement on the discharge of a composite metal foam-phase change material heat exchanger, Int. J. Energy Res. 45 (2) (2021) 2593–2609.
[30] N.B. Khedher, J.M. Mahdi, H.S. Majdi, W.K. Al-Azzawi, S. Dhahbi, P. Talebizadehsardari, A hybrid solidification enhancement in a latent-heat storage system with nanoparticles, porous foam, and fin-aided foam strips, J. Energy Storage 56 (2022), 106070.
[31] X.-H. Han, Q. Wang, Y.-G. Park, C. T'Joen, A. Sommers, A. Jacobi, A review of metal foam and metal matrix composites for heat exchangers and heat sinks, Heat Transfer Eng. 33 (12) (2012) 991–1009.
[32] N. Bianco, S. Busiello, M. Iasiello, G.M. Mauro, Finned heat sinks with phase change materials and metal foams: Pareto optimization to address cost and operation time, Appl. Therm. Eng. 197 (2021), 117436.
[33] V. Joshi, M.K. Rathod, Thermal performance augmentation of metal foam infused phase change material using a partial filling strategy: an evaluation for fill height ratio and porosity, Appl. Energy 253 (2019), 113621.
[34] A. Bahlekeh, H.I. Mohammed, W.K. Al-Azzawi, A. Dulaimi, H.S. Majdi, P. Talebizadehsardari, J.M. Mahdi, CFD analysis on optimizing the annular fin parameters toward an improved storage response in a triple-tube containment system, Energy Sci. Eng. 10 (12) (2022) 4814–4839.
[35] M. Ebrahimnataj Tiji, H.I. Mohammed, R.K. Ibrahem, A. Dulaimi, J.M. Mahdi, M. Keshtkar, P. Talebizadehsardari, Evaluation of T-shaped fins with a novel layout for improved melting in a triple-tube heat storage system, Front. Energy Res. 10 (2022).
[36] M. Kibria, M. Anisur, M. Mahfuz, R. Saidur, I. Metselaar, Numerical and experimental investigation of heat transfer in a shell and tube thermal energy storage system, Int. Commun. Heat Mass Transfer 53 (2014) 71–78.
[37] X. Sun, J.M. Mahdi, H.I. Mohammed, H.S. Majdi, W. Zixiong, P. Talebizadehsardari, Solidification enhancement in a triple-tube latent heat energy storage system using twisted fins, Energies 14 (21) (2021) 7179.
[38] Z.-J. Zheng, Y. Sun, Y. Chen, C. He, H. Yin, Y. Xu, Study of the melting performance of shell-and-tube latent heat thermal energy storage unit under the action of rotating finned tube, J. Energy Storage 62 (2023), 106801.
[39] K. Nedjem, A. Laouer, M. Teggar, E.H. Mezaache, M. Arıcı, K.A. Ismail, Performance enhancement of triplex tube latent heat storage using fins, metal foam and nanoparticles, Int. Commun. Heat Mass Transfer 139 (2022), 106437.
[40] F. Ma, T. Zhu, Y. Zhang, X. Lu, W. Zhang, F. Ma, A review on heat transfer enhancement of phase change materials using fin tubes, Energies 16 (1) (2023) 545.
[41] C. Li, Q. Li, R. Ge, Assessment on the melting performance of a phase change material based shell and tube thermal energy storage device containing leaf-shaped longitudinal fins, J. Energy Storage 60 (2023), 106574.
[42] J.M. Mahdi, F.T. Najim, I.M. Aljubury, H.I. Mohammed, N.B. Khedher, N. K. Alshammari, A. Cairns, P. Talebizadehsardari, Intensifying the thermal response of PCM via fin-assisted foam strips in the shell-and-tube heat storage system, J. Energy Storage 45 (2022), 103733.
[43] S. Zhang, Y. Yao, Y. Jin, Z. Shang, Y. Yan, Heat transfer characteristics of ceramic foam/molten salt composite phase change material (CPCM) for medium-temperature thermal energy storage, Int. J. Heat Mass Transf. 196 (2022), 123262.
[44] M. Ghalambaz, A.A. Melaibari, A.J. Chamkha, O. Younis, M. Sheremet, Phase change heat transfer and energy storage in a wavy-tube thermal storage unit filled with a nano-enhanced phase change material and metal foams, J. Energy Storage 54 (2022), 105277.
[45] D.A. Nield, A. Bejan, Convection in Porous Media, Springer, 2006.
[46] J. Shafi, M. Ghalambaz, M. Fteiti, M. Ismael, M. Ghalambaz, Computational modeling of latent heat thermal energy storage in a Shell-tube unit: using neural networks and anisotropic metal foam, Mathematics 10 (24) (2022) 4774.
[47] X. Yang, P. Wei, X. Wang, Y.-L. He, Gradient design of pore parameters on the melting process in a thermal energy storage unit filled with open-cell metal foam, Appl. Energy 268 (2020), 115019.
[48] Z. Liu, Y. Yao, H. Wu, Numerical modeling for solid–liquid phase change phenomena in porous media: shell-and-tube type latent heat thermal energy storage, Appl. Energy 112 (2013) 1222–1232.
[49] Y. Yao, H. Wu, Interfacial heat transfer in metal foam porous media (MFPM) under steady thermal conduction condition and extension of Lemlich foam conductivity theory, Int. J. Heat Mass Transf. 169 (2021), 120974.
[50] B. Alazmi, K. Vafai, Analysis of variable porosity, thermal dispersion, and local thermal nonequilibrium on free surface flows through porous media, J. Heat Transf. 126 (3) (2004) 389–399.
[51] J.G. Georgiadis, I. Catton, Dispersion in cellular thermal convection in porous layers, Int. J. Heat Mass Transf. 31 (5) (1988) 1081–1091.
[52] Y. Yao, H. Wu, Macroscale modeling of solid–liquid phase change in metal foam/paraffin composite: effects of paraffin density treatment, thermal dispersion, and interstitial heat transfer, J. Therm. Sci. Eng. Applic. 13 (4) (2021).
[53] V. Joshi, M.K. Rathod, Thermal transport augmentation in latent heat thermal energy storage system by partially filled metal foam: a novel configuration, J. Energy Storage 22 (2019) 270–282.
[54] V.V. Calmidi, R.L. Mahajan, Forced convection in high porosity metal foams, J. Heat Transf. 122 (3) (2000) 557–565.
[55] Y. Yao, H. Wu, Z. Liu, Direct simulation of interstitial heat transfer coefficient between paraffin and high porosity open-cell metal foam, J. Heat Transf. 140 (3) (2018).
[56] C. Zhao, J. Wang, Y. Sun, S. He, K. Hooman, Fin design optimization to enhance PCM melting rate inside a rectangular enclosure, Appl. Energy 321 (2022), 119368.
[57] K. Kamiuto, S. San Yee, Heat transfer correlations for open-cellular porous materials, Int. Commun. Heat Mass Transfer 32 (7) (2005) 947–953.
[58] A.I.N. Korti, H. Guellil, Experimental study of the effect of inclination angle on the paraffin melting process in a square cavity, J. Energy Storage 32 (2020), 101726.
[59] A. Agarwal, R. Sarviya, Characterization of commercial grade paraffin wax as latent heat storage material for solar dryers, Mater. Today Proc. 4 (2) (2017) 779–789.
[60] N. Ukrainczyk, S. Kurajica, J. Šipušić, Thermophysical comparison of five commercial paraffin waxes as latent heat storage materials, Chem. Biochem. Eng. Q. 24 (2) (2010) 129–137.
[61] S.-K. Choi, S.-O. Kim, T.-H. Lee, Dohee-Hahn, Computation of the natural convection of nanofluid in a square cavity with homogeneous and nonhomogeneous models, Numer. Heat Transfer A Applic. 65 (4) (2014) 287–301.
[62] H. Zheng, C. Wang, Q. Liu, Z. Tian, X. Fan, Thermal performance of copper foam/paraffin composite phase change material, Energy Convers. Manag. 157 (2018) 372–381.
[63] B. Kamkari, H.J. Amlashi, Numerical simulation and experimental verification of constrained melting of phase change material in inclined rectangular enclosures, Int. Commun. Heat Mass Transfer 88 (2017) 211–219.
[64] B. Kamkari, H. Shokouhmand, F. Bruno, Experimental investigation of the effect of inclination angle on convection-driven melting of phase change material in a rectangular enclosure, Int. J. Heat Mass Transf. 72 (2014) 186–200.